

Spatial-Temporal Heterogeneity of Rock Samples' Deformation and Damage: Experimental Study and Digital Image Correlation Analysis

Fayuan Yan

China University of Mining and Technology - Beijing Campus

Chengzhi Qi (✉ qichengzhi1965@163.com)

Beijing University of Civil Engineering and Architecture

Renliang Shan

China University of Mining and Technology - Beijing Campus

Research Article

Keywords: Rocks, deformation waves, heterogeneity, loading rate, DIC technique

Posted Date: June 15th, 2021

DOI: <https://doi.org/10.21203/rs.3.rs-462119/v1>

License:  This work is licensed under a Creative Commons Attribution 4.0 International License.

[Read Full License](#)

Version of Record: A version of this preprint was published at Applied Sciences on January 27th, 2022.

See the published version at <https://doi.org/10.3390/app12031364>.

1 **Spatial-Temporal Heterogeneity of Rock Samples' Deformation and Damage: Experimental Study and**
2 **Digital Image Correlation Analysis**

3 Fayuan Yan^a, Chengzhi Qi^b, Renliang Shan^a

4 ^aShool of Mechanics and Civil Engineering, China University of Mining & Technology (Beijing) , Beijing 100083,
5 China

6 ^b International cooperation base of Beijing transportation infrastructure construction and Beijing Future Urban
7 Design High-Tech Innovation Center, Beijing University of Civil Engineering and Architecture, Beijing 100044,
8 China

9 *Corresponding Email: qichengzhi1965@163.com (Professor Chengzhi Qi)

10

11 **Abstract:** In-situ observations and laboratory experiments showed that slow deformation waves widely exist
12 in geomedia under loading conditions. Slow deformation waves' behavior exhibits some similarities in media
13 ranging from the scale as large as the Earth's crust to the scale as small as the laboratory test samples. However,
14 the mechanism underlying their generation has not been clarified yet. In this research an experimental study
15 was performed on small-scale red sandstone samples subjected to uniaxial compression at the displacement
16 rates of 0.1, 0.5, and 1 mm/min. Slow deformation waves under different loading rates were analyzed by
17 speckle photography for microscopic characterization combined with the digital image correlation (DIC)
18 technique. The Luders deformation bands were predominantly observed in the flow channels formed at the
19 stage of macro-elastic deformation. The spatial-temporal heterogeneity of the rock sample surface was
20 quantified, and the deformation waves' propagation velocities under different loading rates were obtained. The
21 linear relationship between the propagation velocities of slow deformation waves and the loading rates was
22 determined. The research findings shed some new lights on the evolutionary characteristics of the slow
23 deformation waves.

24 **Keywords:** Rocks; deformation waves; heterogeneity; loading rate; DIC technique

25

26 **1. Introduction**

27 In-situ observations showed that slow deformation waves with propagation velocities much lower than those
28 of transverse and longitudinal waves generated by earthquakes exist in Earth's crust. Slow deformation waves
29 have different names with less essential difference, for example, seismoactive waves (Mogi 1973), creeping
30 stress waves (Savage 1971), tectonic waves (Elsasser 1969; Kasahara 1981), plastic flow waves (Wang 1993;
31 Wang and Zhang 1994) etc. According to the concept of epicenter migration-related waves (Richter 1958),
32 their propagation velocities in the seismic belt may reach only several dozens of kilometers per year (Levina
33 and Ruzhich 2015; Elsasser 1969). The presence of creeping waves can be related to the instability caused by
34 frictional sliding (Ruina 1983). As to the occurrence mechanism of these waves, it is believed that they are
35 jointly triggered by external factors and the changes in the properties of the media in the focal area (Feng 1986).
36 Inside the Earth's crust, there is an interlayer composed of volatile media. Under certain conditions, the
37 propagation of slow deformation waves may be triggered in such volatile media, and they play a crucial role
38 in seismic development and occurrence (Geng and Xu 1990). Studies on the plastic-flow network and plastic
39 flow waves of the continental lithosphere (Wang and Zhang 1994; Wang 1993) have shown that the driving
40 force at the margin of the continental plate is transmitted over a long distance, primarily through the network-
41 like flow and slow deformation waves in the lower lithosphere, including the lower crust and lithospheric
42 mantle. This driving force also controls the intraplate deformation and seismic activities. Under the Indian
43 plate's pushing effect, the deformation flow waves with different quasi-periodicity are present in the central
44 and eastern Asian continent, such as ten-year and one-hundred-year period waves.

45 Deformation and failure of solids under the action of external factors are among the top research concerns
46 in materials science and engineering (Shan et al.2000; Qi et al.2016). In recent years, both the spatial and
47 temporal scales of deformation and failure of solids studied by the researchers have constantly been expanding
48 (Qi et al.2009). (Qi et al.2017) applied the continuous phase transition theory and the Lagrangian mechanics
49 theory to construct a theoretical model of slow deformation waves in rock surrounding deep level tunnel. The
50 scales related to slow deformation waves may range from global to atomic scales, and the types of loading
51 causing the deformation and failure vary from short-term (rapid) loading to long-term one (at creep rates) (Li
52 et al.2008; Li et al.2019). The theoretical study (Li and Shao 2016) applied the multi-microcrack model to

53 study the macroscopic brittle creep failure caused by microcrack growth under step loading and unloading in
54 rocks.

55 During large-scale field observations, significant variations of the geophysical field's spatial-temporal
56 characteristics were measured to determine slow waves' features. It was found that the directional migration of
57 the epicenter was a prevalent phenomenon, which could be observed, for example, in the Hindu Kush region
58 (Malamud and Nikolaevsky 1985,1989), in Baikal Lake region of Siberia (Sherman and Gorbunova 2008;
59 Levina and Ruzhich 2015; Psakhie 2001), and in China (Wang 1987; Wang et al.1990; Wang and Zhang 2004).
60 Fig.1 shows the propagation path of slow deformation waves originated from the Himalayan Arc (Wang 1987).

61 Fig. 1

62 As to the deformation waves at the laboratory level, compression and tensile tests have been performed for
63 the sylvite, marble, and alkali halide samples. The slow deformation waves traveling in the samples were
64 studied (Barannikova et al.2010; Zuev et al.2012). It was found that the slow deformation waves traveling in
65 the rock samples and the alkali halide samples were similar to those observed previously in the metallic
66 materials (Zuev and Danilov 1997). All of these findings are of high significance to the study of slow
67 deformation waves in geomaterials.

68 Most of the existing experimental studies on the slow deformation waves have been conducted on such
69 homogeneous materials as metals or metal halides, but less commonly on rocks. The propagation and evolution
70 characteristics of the deformation waves in rocks have not yet been adequately studied. The microscopic and
71 mesoscopic mechanism of the slow deformation wave has not been clearly explained. The relationship between
72 the propagation speed of the slow deformation wave in the rock and the loading rate has not been specifically
73 studied. Since slow deformation waves mainly propagate in the Earth's crust, typically through rocks as the
74 media, it is important to study their propagation and evolution in rocks. In the present study, indoor uniaxial
75 loading tests were performed for a group of red sandstone samples under the loading rates of 0.1, 0.5, and
76 1mm/min, respectively. In process of deformation and failure of the rock samples, speckle photography
77 technique combined with the digital image correlation (DIC) technique were used to quantify the slow
78 deformation waves. The evolution of the strain component ε_{xx} under the three loading rates was studied, and
79 the propagation rates of the deformation waves under different loading rates were calculated. The relationships

80 between the wave propagation velocity and loading rate were further analyzed. The analysis of obtained
81 nephograms indicated that the Luders deformation occurred predominantly in the flow channels formed at the
82 stage of macro-elastic deformation. It was related to the extreme values of the elastic standing waves.

83

84 **2. Experiments**

85 **2.1 Test equipment and rock samples**

86 The rock samples under study correspond to the third category of the red sandstone. The latter exists in two
87 main structure forms, including granular-clastic and mud cement forms, and has high hygroscopicity, porosity
88 ranging approximately from 0.1 to 0.3, low bonding performance, poor overall performance, and is less prone
89 to disintegration than ordinary sandstone. Nine red sandstone samples with dimensions of
90 50mm×50mm×100mm were prepared using the method recommended by the International Society for Rock
91 Mechanics (ISRM)(Fairhurst and Hudson 1999). Every two opposite sides were parallel to each other, and all
92 of them were smooth. All samples were prepared from the same batch of blocks harvested on-site. Those with
93 defects and joints were eliminated.

94 The rock samples were subdivided into three groups, each containing three samples, and were subjected to
95 displacement-controlled compressive loading at three loading rates, using a DRTS-500 test bench composed
96 of the loading system (with the maximum axial load of 500KN) and the data collection system. The
97 displacement control mode was adopted since the test goal was to investigate slow deformation waves under
98 different loading rates. The rock sample geometry and the experimental equipment are shown in Fig. 2.

99

Fig.2

100 Given that speckle photography was adopted to capture the rock samples' images, the samples were first
101 sprayed with a layer of ordinary white paint and left to dry. Then, another layer of black particle paint was
102 sprayed to form random speckles(Munoz et al.2016; Heinz and Wiggins 2010; Yang et al.2015).

103

104 **2.2. Experimental scheme**

105 Before the main displacement-controlled tests, a group of uniaxial compression tests was first performed to
106 obtain the basic mechanical parameters of rock samples. The average compressive strength of the rock samples

107 was 80 MPa. The loading was imposed under the displacement-controlled mode with three different rates: 0.1,
108 0.5, and 1 mm/min, respectively. In each group, speckle photography was used for microscopic characterization
109 from the start to the end of the loading process. Later, the collected images were subjected to the digital image
110 correlation (DIC) analysis. The evolution of the displacement vector $r(x, y)$ field at the marked points on the
111 sample surface was tracked and recorded to provide data for the further analysis.

112 The stress-strain curves of the rock samples obtained from the uniaxial compression tests are shown in Fig.
113 3, where ε_1 is the axial strain; ε_3 is the transverse strain; and ε_v is the volumetric strain. The pressure in the
114 figure below is defined as positive. A typical stress-strain curve of an intact rock sample can be roughly
115 subdivided into the following four stages. The first stage is the compaction stage, where the curve bends
116 slightly upwards, and the initial microcracks are closed due to the compression. The curve is a straight line at
117 the second stage, so this is the linear elastic stage. At the third stage, the curve bends slightly downwards, and
118 unstable microcracks are generated in the direction parallel to the loading direction. The third stage is called a
119 non-elastic (plastic) stage, while the fourth one is referred to as the failure stage. At the plastic and failure
120 stages, cracks appeared on the sample surface, so the DIC technology would fail to achieve the desired effect.
121 Therefore, DIC is only applicable to the data at the first two (compaction and elastic) stages. In metals and
122 alloys, features of strain localization that resemble those of the deformation waves have been observed at the
123 linear elastic stage in the samples under compression or tension(Danilov et al.2005,2009). In the present study,
124 the deformation waves' propagation velocities at the linear elastic stage (segment AB in Fig. 3) were of the
125 primary concern during the loading process. At this stage, the wave propagation velocity was closer to the slow
126 waves velocities observed in Earth's crust and exhibited similar evolution patterns.

127 Fig. 3

128 **2.3 Technical principle of DIC**

129 Digital image correlation (DIC) technique is a non-contact optical technique known for its practicability and
130 effectiveness (Peters and Ranson 1982). This technology can be used to measure the deformation of an object's
131 surface. Currently, DIC has been widely applied to experimental studies on the deformation of rocks and rock-
132 like materials (Munoz et al.2016; Stirling et al.2013; Lin et al.2019; Miao et al.2018; Lin et al.2019; Zhao et
133 al.2018; Zhou et al.2018). The core algorithm used in the DIC tracks the relative displacement of the speckles

134 by comparing the current image against the reference one, as shown in Fig. 4. The reference image is subdivided
 135 into smaller subsets, whose changes are tracked on the deformation images. The x and y coordinates of the
 136 point $P_{cur} (x_{cur}, y_{cur})$ in the current subset are related to the coordinates of the point $P_{ref} (x_{ref}, y_{ref})$ in the
 137 reference subset as follows:

$$138 \quad x_{cur} = x_{ref} + u_{rc} + \frac{\partial u}{\partial x_{rc}}(x_{ref} - x_{refc}) + \frac{\partial u}{\partial y_{rc}}(y_{ref} - y_{refc}) \quad (1)$$

$$139 \quad y_{cur} = y_{ref} - v_{rc} + \frac{\partial v}{\partial x_{rc}}(x_{ref} - x_{refc}) + \frac{\partial v}{\partial y_{rc}}(y_{ref} - y_{refc}) \quad (2)$$

140 where x_{ref} and y_{ref} are the x and y coordinates of the point P_{ref} in the reference subset, respectively;
 141 x_{refc} and y_{refc} are the x and y coordinates of the central point Q_{ref} in the reference subset, respectively;
 142 u_{rc} and v_{rc} are the horizontal and vertical displacements of the subset, respectively; $\frac{\partial u}{\partial x_{rc}}$, $\frac{\partial u}{\partial y_{rc}}$,
 143 $\frac{\partial v}{\partial x_{rc}}$, and $\frac{\partial v}{\partial y_{rc}}$ are the gradients of the subset's displacement components, respectively.

144 Fig. 4

145 2.4 Calculation of different strain components

146 Different strain components are calculated as follows:

$$147 \quad \nabla r = \beta_{ij} = \begin{vmatrix} \varepsilon_{xx} & \varepsilon_{xy} \\ \varepsilon_{yx} & \varepsilon_{yy} \end{vmatrix} + \omega_z \quad (3)$$

148 where $\varepsilon_{xx} = \frac{\partial u}{\partial x}$ is the strain vector component along the compression direction x , $\varepsilon_{yy} = \frac{\partial v}{\partial y}$ is the transverse strain
 149 component, $\varepsilon_{xy} = \varepsilon_{yx} = \frac{1}{2} \left(\frac{\partial u}{\partial y} + \frac{\partial v}{\partial x} \right)$ is the shear strain component, $\omega_z = \frac{1}{2} \left(\frac{\partial u}{\partial y} - \frac{\partial v}{\partial x} \right)$ is the rotational
 150 component, while u and v are the components of the displacement vector r along the x - and y -axes, respectively.

151 3. Experimental Results

152 3.1 The slow-wave propagation pattern at the compaction stage

153 The rock samples' DIC data were studied at the first (compaction) stage at three loading rates (0.1, 0.5, and
 154 1mm/min). The variation of the strain component ε_{xx} on the sample surface at the initial stage of loading were
 155 analyzed. Here, the 3D diagrams and vertical views of the rock samples under the loading rate of 0.1mm/min
 156 at the two time moments are presented and described in detail. Only the vertical views of the experimental
 157 results under the two loading rates (0.5 and 1mm/min) are presented due to limited space.

158 Fig.5

159 Figure 5 shows the strains at two time moments at the compaction stage under the loading rate of 0.1
160 mm/min. The left side is the end of sample, to which the load was applied. The first column shows the 3D
161 diagrams of strain, from which the strain of the sample could be intuitively observed at a specific time moment
162 for the sample under loading. The second column shows the vertical view of the diagram corresponding to the
163 first column, from which the maximum strain and strain fluctuations along the length of the sample can be
164 obtained. It can be seen from the 3D diagram in Fig. 5a that the irregular strain fluctuations occurred throughout
165 the entire stage. The fluctuations were more significant on the left side and gradually attenuated towards the
166 right one. From the vertical view, it could also be observed that after applying load, strains with more significant
167 fluctuations first appeared on the left side at the initial stage. By contrast, the fluctuations were milder on the
168 right side, and the fluctuations were not synchronized on the left and right sides. At the distance 60-70mm from
169 the left side end, there was an isolated peak of compressive strain. Such fluctuation pattern, which occurred in
170 the form of a single moving peak, resembled a solitary wave or surge wave (Qian 1985), i.e., a gravity wave,
171 which is generally caused by the inertial force and gravity.

172 According to Fig. 5a, the strain values over the entire sample surface fluctuated consistently in the 3D
173 diagram. Except for the leftmost side, there was no significant difference in the strain values within this region.
174 As shown by the vertical view, the strain values fluctuated in a wave-like pattern. However, after the peak at
175 the distance 65 mm from the left side end, the fluctuations were less significant than those on the left side.
176 Although the strain values increased, the fluctuations were obscure and less regular. The strain values were
177 slightly higher at the two ends. In Fig. 5b, several large strain peaks occurred and showed a dispersed
178 distribution. Their spatial distribution was non-uniform and disordered. Compared with Figure 5a, there are
179 several complete wave fluctuations between the 65mm-100mm, and the fluctuations are clear and obvious.
180 According to the vertical views in Fig. 5a and 5b, as loading continued, the fluctuations became more
181 pronounced, and the degree of waviness increased. The peak values gradually increased and occurred more
182 frequently. Moreover, the waviness became increasingly apparent.

183 It is noteworthy that as the loading rate increased, the fluctuations on the left half side became more intensive.
184 The peaks were also greater and denser. At the loading rate of 1 mm/min, the sample surface was subjected to
185 a greater pressure than at other loading rates. As a result, the maximum strain occurred instantaneously in the

186 left corner, its value being approximately five times the strain values at other places on the same surface (Fig.
187 6).

188 Fig. 6

189 Taken together, whatever the loading rate is, the strain component was greater at the end to which the load
190 was applied but smaller at the other end. As the loading continued, the strain components at both ends became
191 more consistent. During this process, the slow deformation wave propagated through the media, accompanied
192 by energy accumulation and conversion. The slow deformation waves were generated by adjusting the
193 imbalance between the driving force and the viscous force inherent inside the solids. This process involved the
194 conversion between the elastic strain and kinetic energies.

195

196 **3.2 Wave characteristics at the same strain under different loading rates**

197 The strain data were analyzed at the strain level of 0.006 under the three loading rates. Figures 7a, 7b, and
198 7c present the 3D strain diagrams under the loading rates of 0.1, 0.5, and 1 mm/min, respectively. The vertical
199 views are compared to the strain diagrams along the sample surface's central line, as shown in Fig. 7.

200 Fig. 7

201 Comparison of the 3D strain diagrams under the three loading rates indicated spatial-temporal heterogeneity
202 and disorderedness. The fluctuations were more significant on the 3D strain diagram under the loading rate of
203 0.1 mm/min (Fig. 7a) than under the other two loading rates. A comparison of the vertical views showed that
204 the deformation waves' peaks were denser on the strain diagrams under the loading rates of 0.1 and 1 mm/min
205 (Fig. 7a and 7c). By contrast, there were much fewer peaks in Fig. 7b, indicating more regular and consistent
206 strain fluctuations on the sample surface. The strain diagrams along the central line of the sample surface were
207 analyzed under the three loading rates. The fluctuation is obvious from the left boundary to 65mm in Fig. 7a.
208 However, the fluctuations barely existed in the second half, indicating that the deformation wave had not yet
209 propagated to the second half. By contrast, the fluctuation in Figure 7c is not so regular, and there is no obvious
210 fluctuation period. As compared with the cases of other two loading rates, the waves undulates gently. Thus,
211 the deformation waves' fluctuations were much more regular in the red sandstone samples under the loading
212 rate of 0.5 mm/min. The propagation rate was the lowest at the loading rate of 0.1 mm/min. And at 1 mm/min,
213 the deformation wave propagates in the form of broken lines.

214

215 3.3 Strain nephograms of the deformation waves

216 Fig .8

217 Fig. 9

218 Four time moments at the compaction and elastic stages were chosen during the loading process (see Fig.
219 8). The strain nephograms of the three strain components ε_{xx} , ε_{yy} and ε_{xy} are presented at these four time
220 moments, as shown in Fig. 9. For data processing, negative strain values under compression were represented
221 by blue and light blue in the nephograms, while positive strain values under tension were represented by red
222 and yellow. As indicated by the strain component ε_{xx} , the micro-grains on the sample surface prior to loading
223 were in a disordered and dispersed state. During the compression process, there was a region of tensile
224 deformation between the regions of compressive deformation. As the loading continued, these micro-grains
225 near flow channels moved closer to the flow channels (at an angle of about 60° relative to the x -axis, i.e., the
226 sample axial direction. Points 1 and 2, represented by dotted lines in Fig. 9) and gradually became connected
227 along the flow channels. These flow channels cross symmetrically with each other and are distributed in a grid
228 pattern.

229 Throughout the loading process, the values of the strain components ε_{yy} and ε_{xy} were very small. Among
230 them, the distribution of ε_{yy} cloud image shows obvious vertical distribution characteristics, and gradually
231 shifts to the middle with the loading time. The areas on both sides of the ε_{xy} strain cloud map show periodic
232 strong tensile deformation zones from the beginning. For example, in the nephograms (Fig. 9), corresponding
233 to points 2 and 3 in Fig. 8, the strong tensile deformation, as indicated by the strain component ε_{xy} , periodically
234 appeared at 20-60mm, with a magnitude of about 0.1% (as indicated by the arrowhead at the point 3 in Fig. 9).
235 These regions of strong tensile deformation corresponded to the flow channels observed in the nephogram of
236 ε_{xx} . This phenomenon was observed throughout the compaction and elastic stages of loading.

237 As observed in the nephogram of ε_{xx} , the nucleation of Luders bands (LB), i.e., shear bands formed in
238 regions of stress concentration, occurred during the loading process (point 2 in Fig. 9). At first, the nuclei had
239 small oval cross-sections and appeared in pairs. One of them was a region of compressive strain with the
240 maximum strain value being -0.5%; the other was a region of tensile strain with the maximum strain value
241 being 0.2%. The grain deformation and LB nucleations were more conspicuous in the nephogram of ε_{xy} and
242 observed roughly at the same positions as those in the nephogram of ε_{xx} . The maximum strain value was
243 0.15%. The observed nucleation pattern can be explained as follows. The displacements originated from the

244 sample surface, whose deformation exceeded the bulk one, i.e., the average deformation of the sample. During
245 the sample's loading-induced deformation, the displacement was rapidly released, thereby resulting in the LB
246 nucleation.

247 After grain deformation and LB nucleation, the Luders bands were gradually formed. In the beginning, the
248 Luders bands were obscure. As the loading continued, the Luders bands became clearer and began to show
249 more conspicuous banding features. This trend started from both sides of the sample simultaneously, with slow
250 interconnection and penetration in the transverse direction. This phenomenon indicated that the Luders bands
251 were already formed (points 3 and 4 in the nephogram of ε_{xx} in Fig. 9) before the plastic deformation stage.
252 The Luders bands were mainly concentrated on the half part of the sample near the end where the load was
253 applied; however, the strain was smaller on the other half part. This situation was not observed on the
254 nephograms of ε_{yy} and ε_{xy} .

255 On the nephogram of the ε_{xy} component near the left side of the sample, the strain concentration were
256 periodically distributed at an interval of about 10 mm (as indicated by the arrowheads at points 1 and 2 in Fig.
257 9). The deformation (probably, a plastic one) at these central points was about 0.5%. Between these points,
258 there were points with the opposite sign of ε_{xy} component, which were treated as nodes of elastic standing
259 waves in the samples under loading (points of maximum and minimum values). The points marking the flow
260 channels and the nodes of elastic standing waves that appeared at the compaction and linear elastic stages
261 remained active throughout the entire loading process. This indicated the conversion between the plastic and
262 elastic deformation standing waves.

263 As to the component ε_{xx} , the flow channels were parallel to the Luders bands. However, the Luders bands
264 and the initial stress concentrators (i.e., nucleation sites) were located outside the flow channels. From this, we
265 inferred that they were of different origins.

266 Fig. 10

267 Three points were chosen along the sample's axis, namely, at 30, 50, and 70 mm (positions of these points
268 are shown in the nephogram of ε_{xx} at point 3 in Fig. 9). The temporal variations of the axial strain components
269 at these three points during the loading process were tracked and represented, as shown in Fig. 10. The curves
270 in Fig. 10 depict fluctuations of the vertical strain component during the loading process. Generally speaking,

271 the deformation is greater near the end when the load was applied and smaller farther away from this end. At
272 30 mm, $0.3\% < \epsilon_{xx} < 0.35\%$; at 50mm, $0.35\% < \epsilon_{xx} < 0.4\%$; at 70mm, $0.4\% < \epsilon_{xx} < 0.48\%$. These three points were
273 close to the three flow channels generated during the loading process (Fig. 9).

274 Thus, the maximum deformation amplitudes of the three flow channels can be ranked as follows:
275 $\epsilon_{xx}^{max}(FC1) > \epsilon_{xx}^{max}(FC2) > \epsilon_{xx}^{max}(FC3)$. They are determined by their duration. The longer the time it appears,
276 the greater its deformation. As the width of the Luders bands increased, these three flow channels successively
277 entered active deformation regime. Therefore, it was presumed that the Luders bands' formation was related to
278 the flow channels' maximum strain value. As the deformation was intensified, the Luders bands interacted with
279 the flow channels nearby to generate the maximum strain values.

280

281 **3.4 Propagation velocity analysis of the deformation waves at the elastic stage**

282 Deformation waves are generated during the loading process of the red sandstone samples. Some researchers
283 have studied the propagation of deformation waves and estimated their propagation velocity range. However,
284 the relationships between the propagation velocities of the deformation waves and the loading rates have not
285 been fully clarified. In our study, such relationships were determined based on the experimental data.

286 Deformation waves has one unique feature: it propagates along the sample's axis. The loading diagram is
287 shown in Fig. 11. Since the samples were loaded at a steady loading rate, an approximate dependence $\epsilon \sim t$
288 assumed. The deformation waves' strain peaks (i.e., peaks and troughs of the deformation waves) were plotted
289 on the X -axis. The slope of the straight line representing the relationship of X vs. t was calculated. On this basis,
290 the motion velocities of points with the maximum and minimum values of strain, that is, the propagation
291 velocities of the deformation waves, were estimated.

292 Fig. 11

293 Taking the case with a loading rate of 0.5 mm/min as an example. After the microscopic characterization of
294 the specimen, the deformation diagram of the strain component ϵ_{xx} on the centerline at 8 time moments was
295 selected in the elastic stage (Fig.12). According to the treatment method of local strain maximization, the points
296 of local strain maximum are chosen for comparative analysis. The results are shown in Fig. 13.

297 Fig. 12

298 Fig. 13

299 After data processing, the deformation wave's propagation velocities were estimated as 5.4×10^{-5} , 6.0×10^{-5} ,
300 and 6.3×10^{-5} m/s in the three groups of experiments under the loading rate of 0.5 mm/min. After averaging, the
301 strain peak's propagation velocity (of deformation waves) was 5.9×10^{-5} m/s in the samples. It exceeded the
302 axial boundary advance propagation velocity of 0.8×10^{-6} m/s (equivalent to the loading rate of 0.5 mm/min)
303 by one order of magnitude. Therefore, the propagation velocities of the deformation waves was significantly
304 higher than that of the matter particles.

305 The propagation velocity of the slow deformation waves was calculated under the loading rate of 0.5mm/min.
306 Under this loading rate, stable regions of localized deformation were formed due to the slow deformation waves.
307 These regions did not move over time. It can be observed from the dashed box in Fig. 12 that at 60-100 mm on
308 the sample surface, the peaks and troughs' positions were relatively fixed, and the peak and the basic shape of
309 the wave only change slightly. However, the waveform and the peaks' positions changed significantly for the
310 regions formed at an earlier stage, indicating the normal propagation and fluctuations. This situation persisted
311 until the last diagram. The above region was stable and no longer experienced dramatic plastic deformation
312 over time. The propagation of slow deformation wave occurs at the initial stage of loading, that is, the elastic
313 stage and the compaction stage. At the initial stage, the damage of the sample develops uniformly, and the
314 slow deformation wave propagation is produced. As the loading process goes on, the plastic localization occurs
315 gradually, and the propagation of slow deformation wave no longer appears. At this stage, the plastic
316 deformation is concentrated to the adjacent weak points, thus showing the plastic localization, and then these
317 weak points are gradually connected, resulting in the fracture of a plane.

318 Using the same method, the propagation velocities of the deformation waves in the three groups of samples
319 under the loading rate of 0.1mm/min were estimated as 3.0×10^{-5} , 3.3×10^{-5} , and 3.5×10^{-5} m/s, respectively. The
320 average wave propagation velocity was 3.27×10^{-5} m/s. Under the loading rate of 1 mm/min, the propagation
321 velocities of the deformation waves in the three tested samples were 10.1×10^{-5} , 10.5×10^{-5} , and 10.7×10^{-5} m/s,
322 respectively, and the average velocity was 10.4×10^{-5} m/s. The wave propagation velocities under the three
323 loading rates were roughly equivalent to those of the plastic flow waves controlling earthquake migration in
324 the lower lithosphere (Wang 1994).

325 The deformation waves' propagation velocities obtained at the loading rates of 0.1, 0.5, and 1 mm/min by
326 testing nine samples are plotted in Fig.14. As the loading rate increases, the propagation velocities of the
327 deformation waves increases linearly. Thus, a positive linear correlation between these parameters with a high
328 correlation coefficient $R^2=0.9964$ was revealed. The above dependence was best-fitted by a linear regression
329 formula presented in Fig.14.

330 Fig. 14

331 4. Discussion

332 Various experimental tools tracked the spatial-temporal occurrences of the deformation waves in the
333 deformed red sandstone samples during their loading. The generation of deformation waves in the rock samples
334 was found to be related to the regions of elastic stress concentration of varying scales (Farber et al.2019). Under
335 the three loading rates, the deformation waves' propagation rates were 3.0×10^{-5} , 5.9×10^{-5} , and 10.4×10^{-5} m/s,
336 respectively. They exceed by one order of magnitude the axial loading rates, i.e., the boundary advance speeds,
337 of 0.16×10^{-6} , 0.8×10^{-6} , and 1.6×10^{-6} m/s, respectively, for the loading rates of 0.1, 0.5, and 1 mm/min. Thus,
338 the propagation rate of deformation waves is significantly higher than that of the mass particles. The local
339 thickening and uplift caused by boundary advancement continue to propagate with the help of elastic force and
340 inertial force. Thus, the matter particles' initial high displacement rate under the elastic force's action tended to
341 decrease due to viscous resistance. As the flow rate decreased, the subsequent substance deformation was
342 accumulated, leading to local bulging and increased elastic potential. This would further accelerate the matter
343 particles' displacement velocity. Such alternation of high and low velocities is manifested as wave propagation.
344 It can be considered that this is a kind of deformation wave that contains the migration of matter particles which
345 is essentially the particle momentum waves proposed by Fitzgerald (1966),

346 The deformation wave propagation is a process of mutual conversion between the elastic and kinetic energies
347 under the boundary-driven condition and a process of adjustment for the imbalance between the driving force
348 and viscous force inherent in solids. The situation where the driving boundary induces the deformation wave
349 propagation is known as "boundary-driven wave generation" or "external-driven wave generation". Viscous
350 deformation arises when the elastic stress is relaxed in regions of stress concentration (Farber 2002). The
351 elastic strain concentration is restricted by viscous deformation (relaxation). Moreover, since the viscous

352 deformation is usually induced near the regions of stress concentration, the distribution of centers of viscous
353 deformation (flow channels) in the samples coincided with those of the regions of elastic strain concentration.
354

355 **5. Conclusions**

356 In the present study, rock samples were subjected to microscopic characterization by speckle photography
357 during the uniaxial compression test. The image processing via the DIC technology revealed the spatial-
358 temporal evolution of the deformed samples' deformation waves. The characteristics of deformation waves in
359 the samples under loading were obtained as follows:

360 (1) The deformation waves slowly propagated from one end of the sample, to which the load was applied.
361 The strain magnitude was much higher at one end to which the load was applied than that at the other one at
362 the beginning of loading. However, the strain values became comparable over time over the sample, thus
363 demonstrating deformation wave propagation in the laboratory tests of small-scale rock samples.

364 (2) In the samples under loading, the deformation waves are influenced by the elastic standing waves, which
365 could be inferred from the positions of the minimums and maximums of the elastic standing waves (regions of
366 stress concentration) and the flow channels' distributions. These flow channels were formed at the compaction
367 and elastic stages and were involved in the subsequent stages. As the stress increased, the LB nuclei interacted
368 with the flow channels nearby to generate the minimum and maximum strain values (ϵ_{xx}).

369 (3) As the loading rate increased, the propagation velocity of the deformation waves increased linearly. Thus,
370 a positive linear correlation between these parameters with a high correlation coefficient $R^2=0.9964$ was
371 revealed.

372 (4) The experiments and comparative analyses conducted in this paper were semi-quantitative ones, and
373 further investigations are needed in this respect. The research findings shed some new lights on the evolutionary
374 characteristics of slow deformation waves and earthquake migration. They also provide experimental data for
375 more in-depth analysis of the generation and propagation mechanism of slow deformation waves in the
376 continental plates.

377
378 **Acknowledgments**

379 This work was supported by the National key basic research development plan (approval No.:
380 802015CB575), National Natural Science Foundation of China (approval No.: 51774018), and Yangtze River
381 scholars innovation team program (PCSIRT, IRT_17R06).

382 **Data Availability Statement**

383 Some or all data, models, or code that support the findings of this study are available from the corresponding
384 author upon reasonable request.

385 **References**

- 386 Brace WF, Paulding BW, Scholz C (1966) Dilatancy in fracture of crystalline rocks. *Journal of Geophysical*
387 *Research* 71(16):3939-3953
- 388 Barannikova SA, Nadezhkin MV, Zuev LB et al (2010) On inhomogeneous straining in compressed sylvinitite .
389 *Technical Physics Letters* 36(6):507–510
- 390 Blaber J, Adair B, Antoniou A (2015) Ncorr: open-source 2D digital image correlation matlab software.
391 *Experimental Mechanics* 55:1105–1122
- 392 Danilov VI, Konovalov SV, Zhuravleva SV et al (2005) Macrolocalization of plastic strain in creep of fine-
393 grain aluminum. *Technical Physics* 50(3):376-379
- 394 Danilov VI, Orlova DV, Zuev LB et al (2009) Special features of the localized plastic deformation and fracture
395 of high-chromium steel of the martensitic class. *Russian Physics Journal* 52(5):525-531
- 396 E. R. Fitzgerald (1966) Particle waves and audio frequency modes in crystals. *J. Acoust. Soc. Amer.* Part 1,
397 1856–1869
- 398 Elsasser W (1969) Convection and stress propagation in the upper mantle. In: *The application of modern*
399 *physics to the Earth and planetary*, New-York: Wiley 223–246
- 400 Feng DY (1986) Study of seismicity waves, world seismological translation No.2 (in Chinese)
- 401 Fairhurst CE, Hudson JA (1999) Draft ISRM suggested method for the complete stress-strain curve for intact
402 rock in uniaxial compression. *International Journal of Rock Mechanics and Mining Sciences and*
403 *Geomechanics Abstracts* 36:281–289
- 404 Farber VM (2002) Contribution of Diffusion Processes to Structure Formation in Intense Cold Plastic
405 Deformation of Metals. *Metal Science and Heat Treatment* 44(7-8):317-323

406 Farber VM, Polukhina ON, Vichuzhanin DI et al (2019) A Study of Plastic Deformation of 08G2B Steel Before
407 and at the Yield Plateau by Digital Image Correlation Technique. Part 1. Formation of Plastic and Elastic
408 Deformation Waves. *Metal Science and Heat Treatment* 61(5-6):274-279

409 Fu B, Hu L, Tang C (2020) Experimental and numerical investigations on crack development and mechanical
410 behavior of marble under uniaxial cyclic loading compression. *International Journal of Rock Mechanics
411 and Mining Sciences* 130:104289

412 Geng NG, Xu DJ (1990) Plastic deformation waves in fault gouge observed in field large scale friction
413 experiments . *Acta seismologica Sinica* (01): 45-49 (in Chinese)

414 Heinz SR, Wiggins JS (2010) Uniaxial compression analysis of glassy polymer networks using digital image
415 correlation. *Polym Testing* 29:925–932

416 Kasahara K. (1981) *Earthquake mechanics*. Cambridge University Press, Cambridge, UK

417 Li SC, Wang HP, Qian QH et al (2008) In situ monitoring study on zonal cracking of surrounding rock in deep
418 roadway. *Journal of rock mechanics and engineering* 27(8): 1446-1553 (in Chinese)

419 Levina EA, Ruzhich VV (2015) The seismicity migration study based on space-time diagrams. *Geophysics and
420 Tectonophysics* 6(2):225-240 (In Russian)

421 Li XZ, Shao ZS (2016) Investigation of Macroscopic Brittle Creep Failure Caused by Microcrack Growth
422 Under Step Loading and Unloading in Rocks. *Rock Mechanics and Rock Engineering* 49(7): 2581-2593

423 Lin Q, Wan B, Wang SQ et al (2019) Visual detection of a cohesionless crack in rock under three-point bending.
424 *Engineering Fracture Mechanics* 211:17–31

425 Li XZ, Qu XL, Qi CZ et al (2019) A unified analytical method calculating brittle rocks deformation induced
426 by crack growth. *International Journal of Rock Mechanics and Mining Sciences* 113:134-141

427 Lin H, Yang HT, Wang YX et al (2019) Determination of the stress field and crack initiation angle of an open
428 flaw tip under uniaxial compression. *Theoretical and Applied Fracture Mechanics* 104:1–13

429 Mogi K.(1973) Relationship between shallow and deep seismicity in the western Pacific region. *Tectonophysics*
430 17 (1–2), 1–22

431 Malamud AS, Nikolaevsky VN (1985) Cyclicity of seismic tectonic events in the border of Indian lithosphere
432 plate. *Reports of USSR AS* 283(6):1333-1337 (in Russian)

433 Malamud AS, Nikolaevsky VN (1989) Earthquake cycles and tectonic waves. Donish, Dushanbe

434 Martin CD, Chandler NA (1994) The progressive fracture of lac du bonnet granite. International Journal of
435 Rock Mechanics and Mining Sciences and Geomechanics Abstracts 31:643–659

436 Munoz H, Taheri A, Chanda EK (2016) Pre-peak and post-peak rock strain characteristics during uniaxial
437 compression by 3D digital image correlation. Rock Mechanics and Rock Engineering 49:2541–2554

438 Miao S, Pan PZ, Wu Z et al (2018) Fracture analysis of sandstone with a single filled flaw under uniaxial
439 compression. Engineering Fracture Mechanics 204:319–343

440 Peters WH, Ranson WF (1982) Digital imaging techniques in experimental stress-analysis. Kluwer Law
441 International 21:427–431

442 Psakhie SG, Ruzhich VV, Smekalin OP et al (2001) Response of the geological media to dynamic loading.
443 Physical Mesomechanics 4(1):67-71 (in Russian)

444 Qian LX (1985) Encyclopedia of China. Mechanics. Beijing: China Encyclopedia press (in Chinese)

445 Qi CZ, Wang MY, Qian QH (2009) Evolution of the deformation and fracturing in rock masses near deep-level
446 tunnels[J]. Journal of Mining Science 45(2):112-119

447 Qi CZ, Wang MY, Bai JP et al (2016) Investigation into size and strain rate effects on the strength of rock-like
448 materials. International Journal of Rock Mechanics and Mining Sciences 86:132-140

449 Qi CZ, Chen HX, Chanyshv A et al (2017). Modeling deformation wave in rock near deep level tunnel .
450 Journal of Mining Science 53(6):1025-1036

451 Richter CF (1958) Elementary seismology W.H. Freeman, San Francisco

452 Ruina A (1983) Slip instability and state variable friction laws-Ruina-2012 Journal of Geophysical Research
453 Solid Earth 88(B12):10359-10370

454 RenLiang S, YuSheng J, BaoQiang L (2000) Obtaining dynamic complete stress–strain curves for rock using
455 the Split Hopkinson Pressure Bar technique. International Journal of Rock Mechanics and Mining Sciences
456 37(6):983-992

457 Savage J.A.(1971) A theory of creep waves propagation along a transform faults. Journal of Geophysical
458 Research 76 (8), 1954–1966

459 Sherman SI, Gorbunova EA (2008) Wave origin of fault activation in central Asia on the basis of seismic
460 monitoring . *Physical Mesomechanics* 11(1):115-122 (in Russian)

461 Stirling RA, Simpson DJ, Davie CT (2013) The application of digital image correlation to brazilian testing of
462 sandstone. *International Journal of Rock Mechanics and Mining Sciences* 60:1–11

463 Wang JM (1987) The Fenwei rift and its recent periodic activity .*Tectonophysics* 133 (3–4):257–275

464 Wang M, Guo J, Qin F (1990) Seismicity of North China and its relation with movements at major faults, In:
465 Moiseenko V.G., Zagruzina I.A. (Eds.), *Deep structure of the Pacific ocean margin, Proceedings of the*
466 *International Symposium. Amur KNII, Blagoveshchensk Part 2:60–73*

467 Wang SZ (1993) Brittle ductile transition and plastic flow network of rocks. *Progress in geophysics* (04): 25-
468 37 (in Chinese)

469 Wang SZ, Zhang ZC (1994) Intraplate plastic flow waves and seismic migration (1). *Seismogeology* (04): 289-
470 297 (in Chinese)

471 Wang SZ, Zhang ZC (2004) Plastic-flow waves(‘slow waves’) and seismic activity in Central-Eastern Asia.
472 *Seismology and Geology* 26 (1):91–101 (in Chinese)

473 Yang G, Cai ZX, Zhang XC et al (2015) An experimental investigation on the damage of granite under uniaxial
474 tension by using a digital image correlation method. *Optics and Lasers in Engineering* 73:46–52

475 Zuev LB, Danilov VI (1997) Plastic deformation viewed as evolution of an active medium. *International*
476 *Journal of Solids and Structures* 34:3795-3805

477 Zuev LB, Danilov VI (1997) Plastic deformation modeled as a self-excited wave process at the maso- and
478 macro-level . *Theoretical and Applied Fracture Mechanics* 30(3):175-184

479 Zuev LB, Barannikova SA, Zhigalkin VM et al (2012) Laboratory observation of slow movements in rocks.
480 *Journal of Applied Mechanics and Technical Physics* 53(3):467-470

481 Zhao C, Zhou YM, Zhao CF et al (2018) Cracking processes and coalescence modes in rock-like specimens
482 with two parallel pre-existing cracks. *Rock Mechanics and Rock Engineering* 51:3377–3393

483 Zhou XP, Lian YJ, Wong LN et al (2018) Understanding the fracture behavior of brittle and ductile multi-
484 flawed rock by uniaxial loading by digital image correlation. *Engineering Fracture Mechanics* 199:438–
485 460

Figures

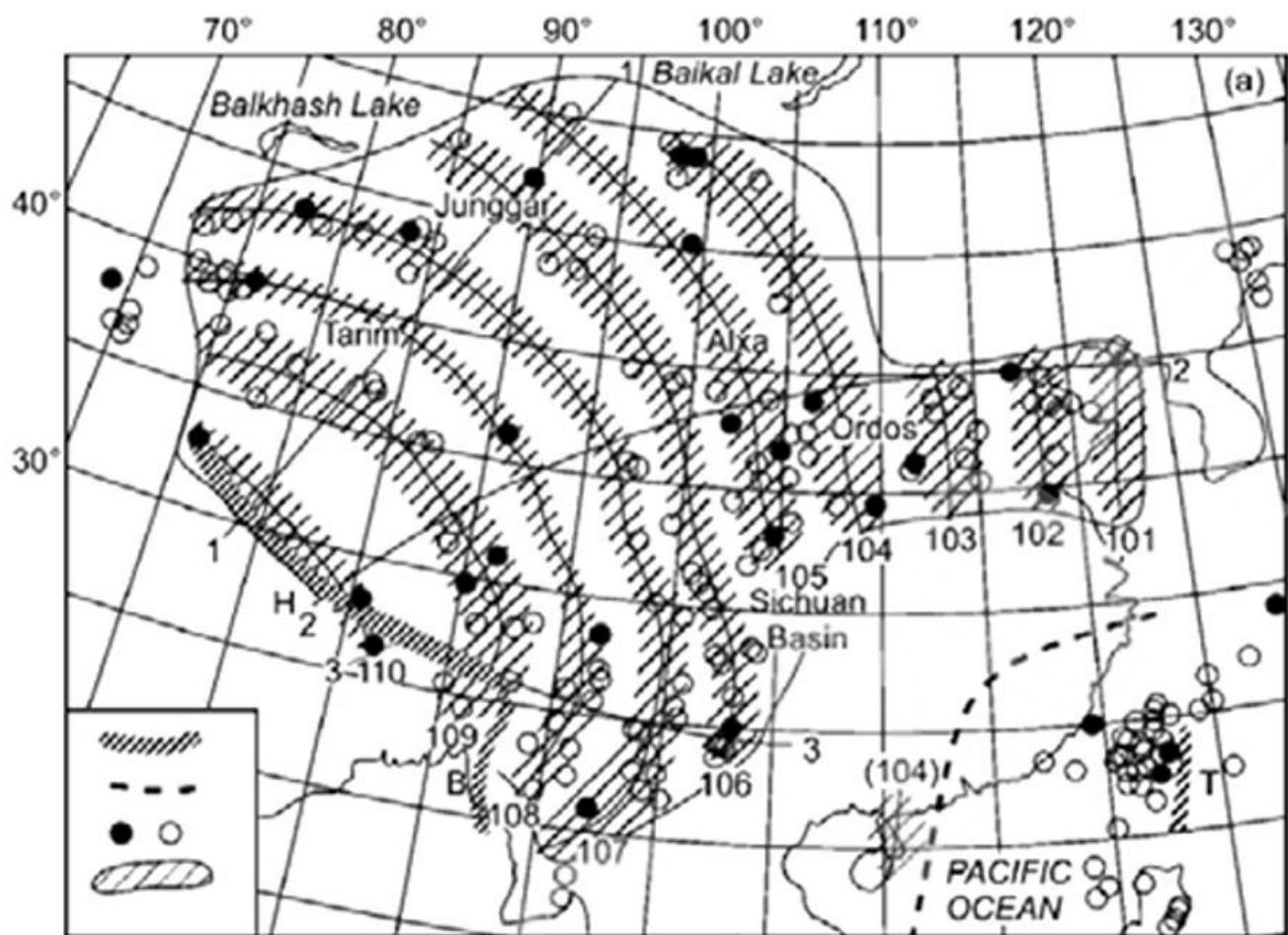


Figure 1

Propagation of slow waves originated from the Himalayan Arc in the East Asian continent (Wang 1987, Wang et al. 1990) Note: The designations employed and the presentation of the material on this map do not imply the expression of any opinion whatsoever on the part of Research Square concerning the legal status of any country, territory, city or area or of its authorities, or concerning the delimitation of its frontiers or boundaries. This map has been provided by the authors.



(a)

(b)

(c)

Figure 2

Red sandstone samples and relevant experimental equipment (a) The rock samples, (b) Loading and speckle photography system, (c) Local image of loading

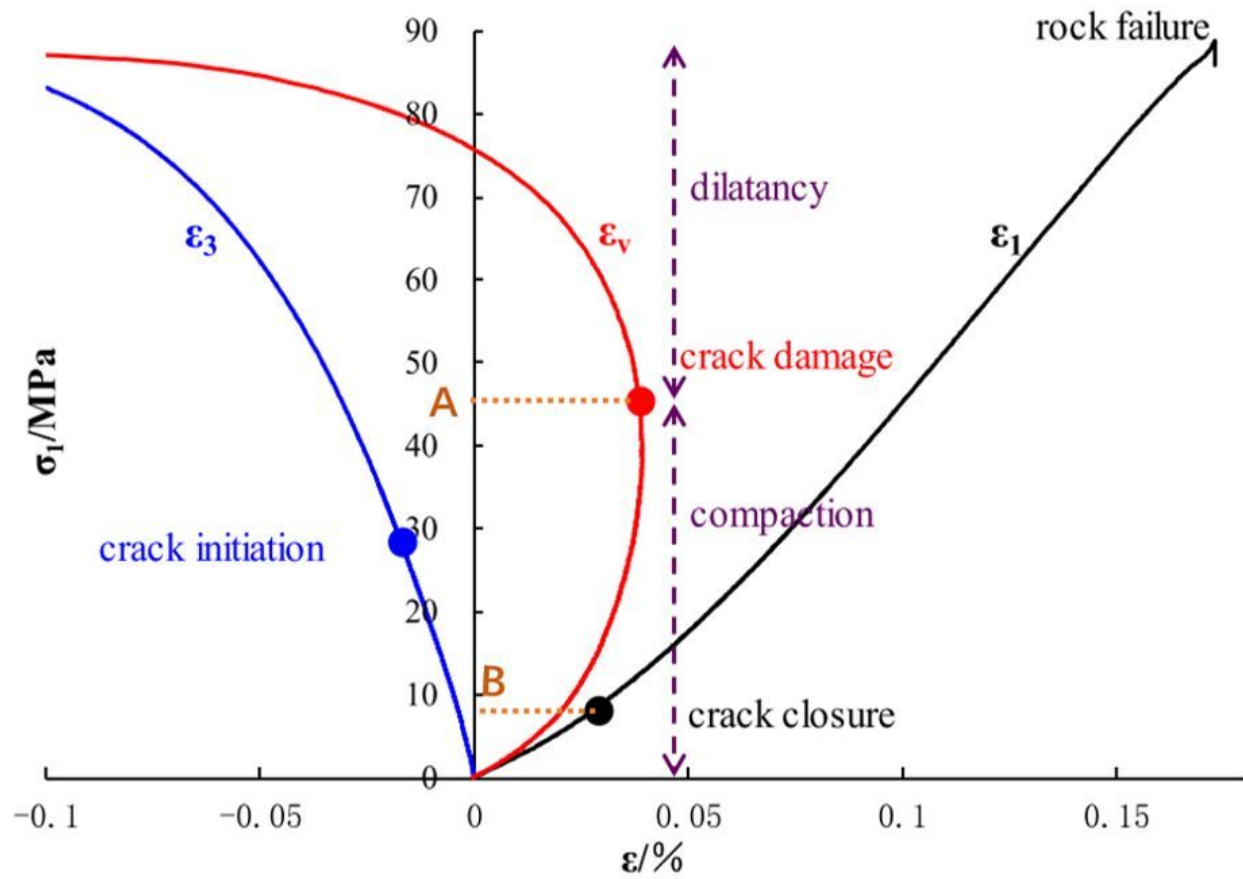


Figure 3

Stress-strain curves of the rock samples and the corresponding stress thresholds (Brace et al. 1966, Martin and Chandler 1994, Fu et al. 2020)

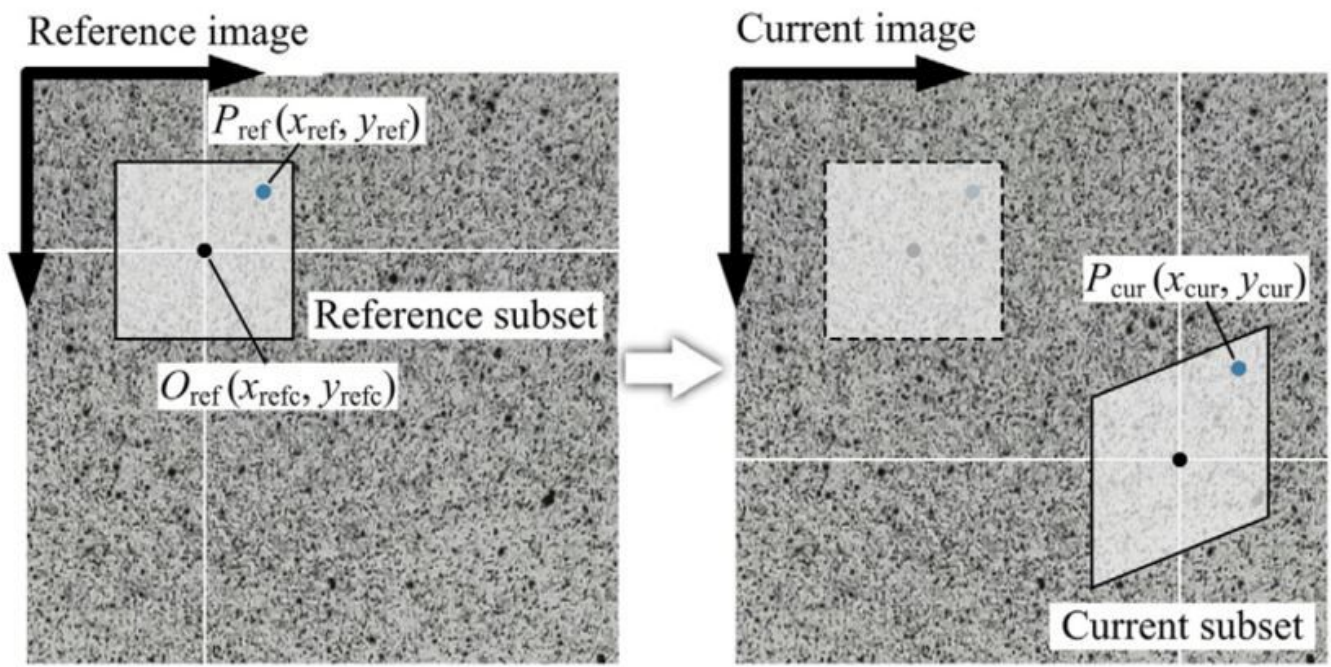


Figure 4

Schematic of the DIC technology (Blaber et al. 2015)

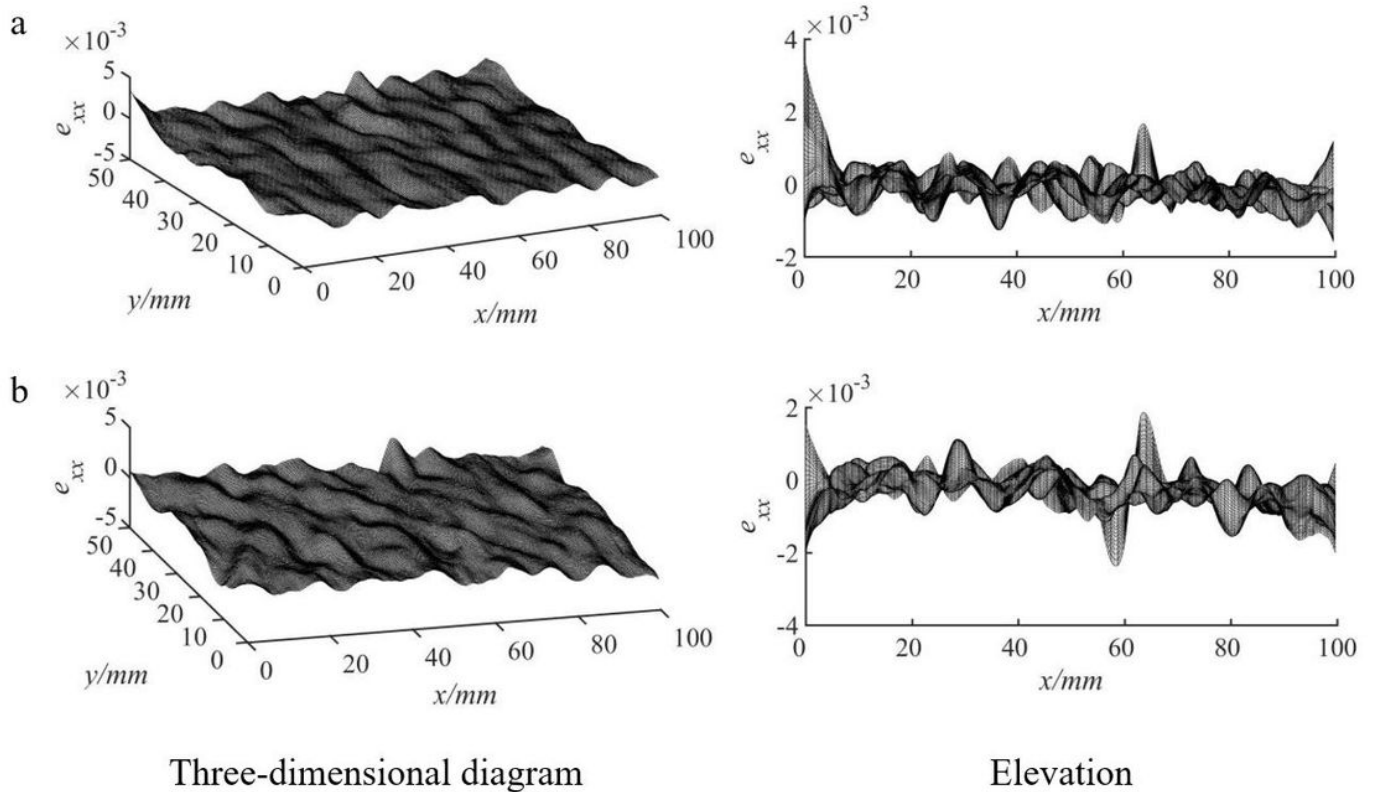


Figure 5

Strain characterization of the rock samples at different time points under the loading rate of 0.1mm/min

Deformation wave elevation of strain component ϵ_{xx}

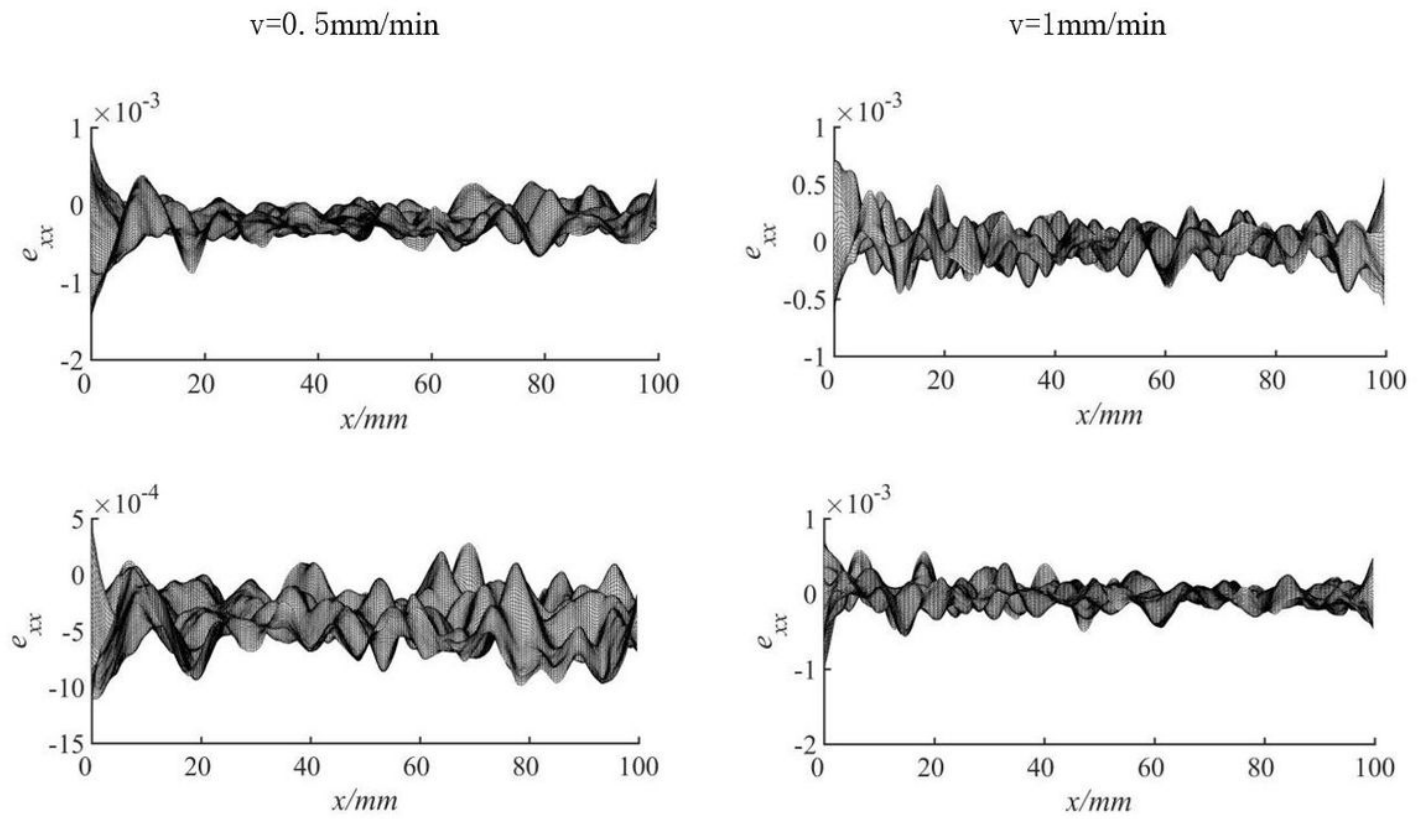


Figure 6

Vertical view of the strain component ϵ_{xx} at different time points at loading rates of 0.5 and 1 mm/min

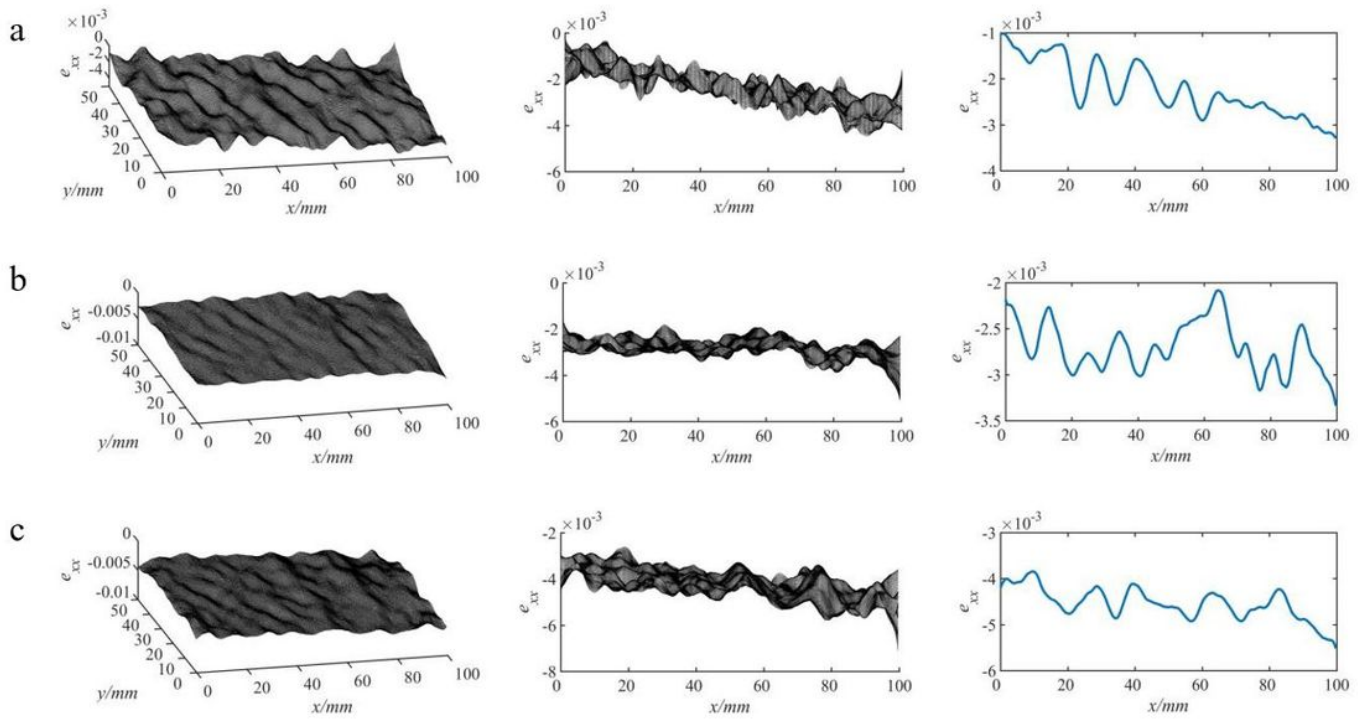


Figure 7

Strain diagrams at the same strain under different loading rates

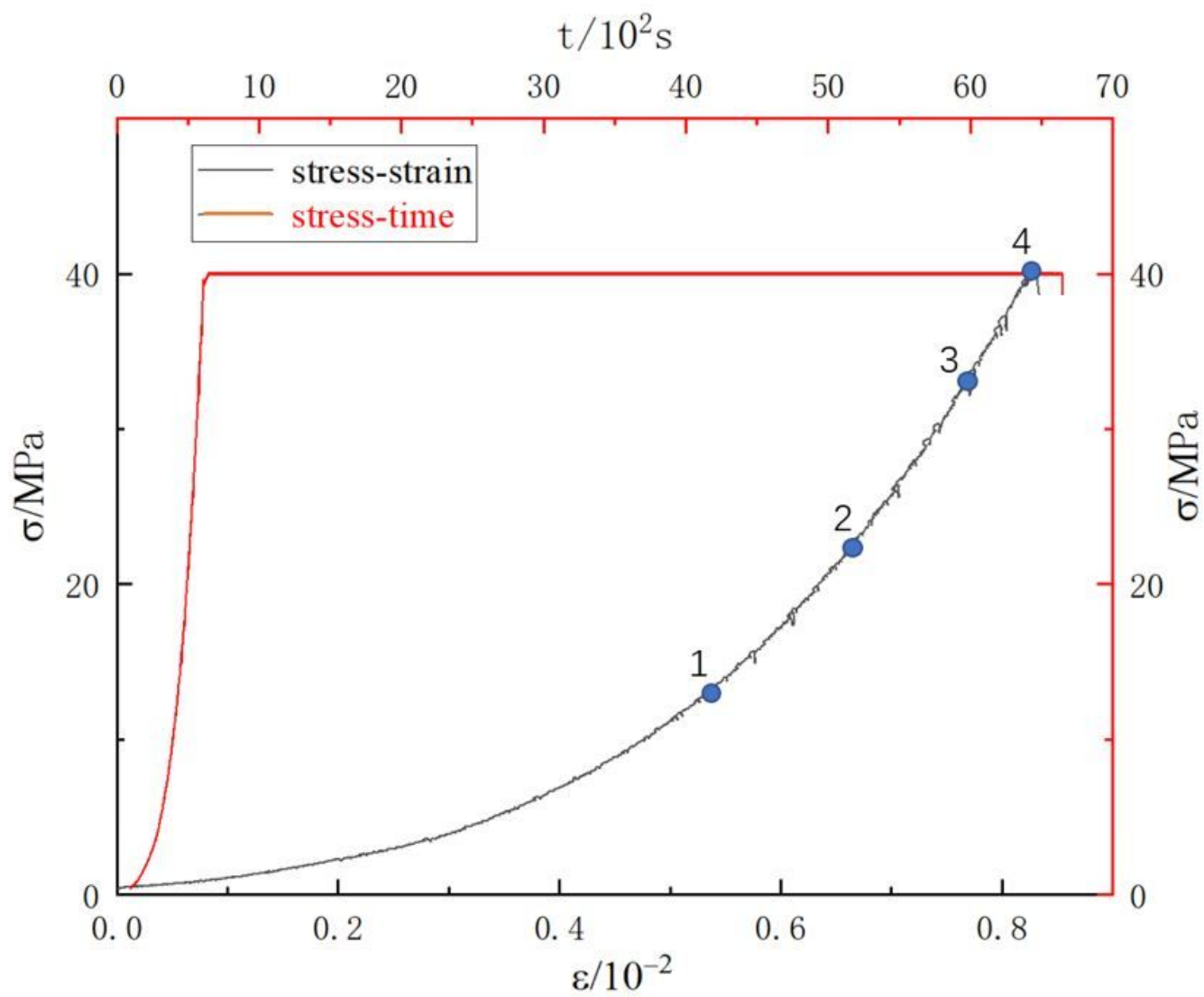


Figure 8

Stress-strain and stress-time curves at a loading rate of 0.1 mm/min

Loading sampling point at 1mm/min

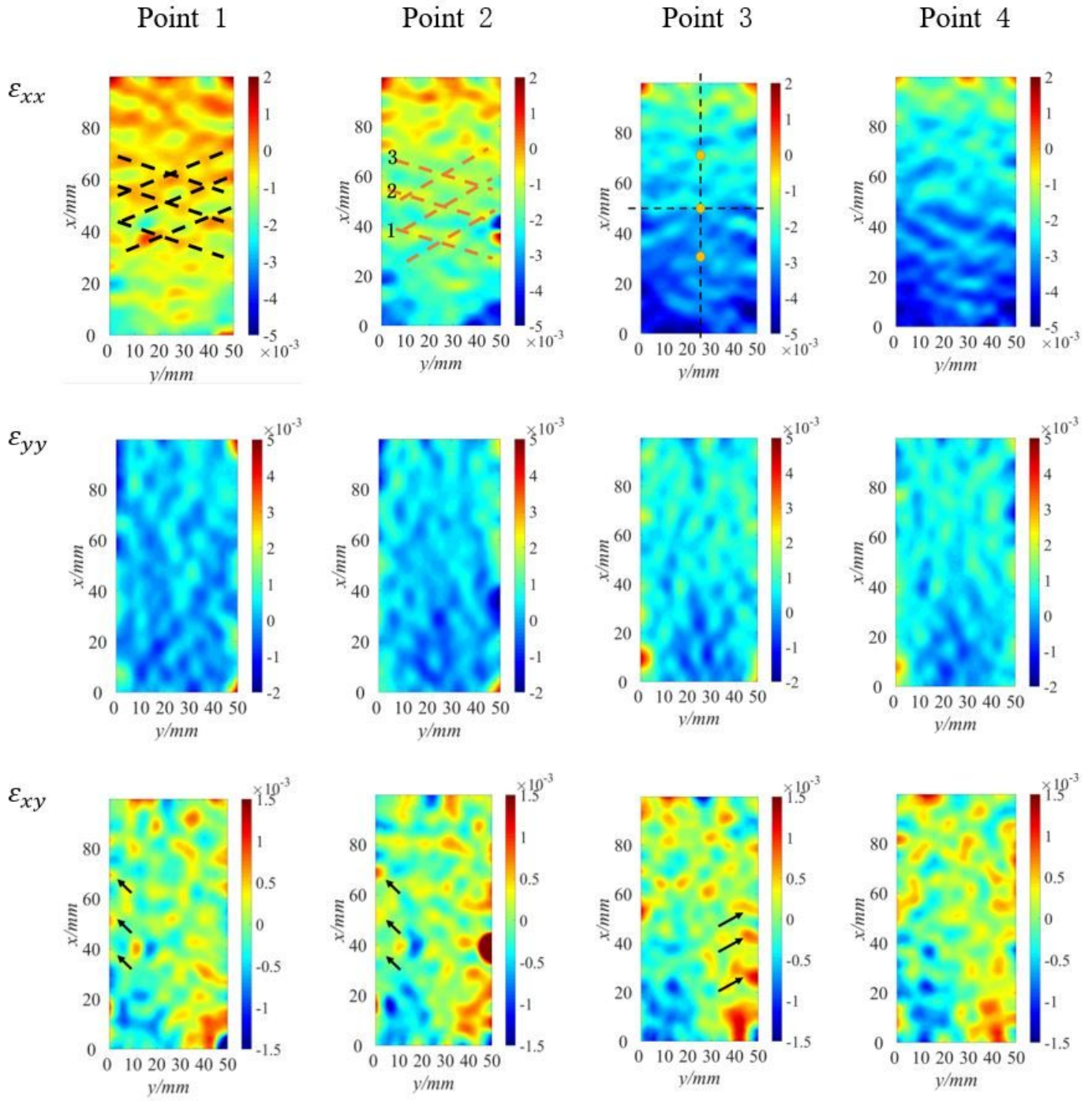


Figure 9

Strain nephograms corresponding to points 1 to 4 of the stress-strain curve in Fig. 8

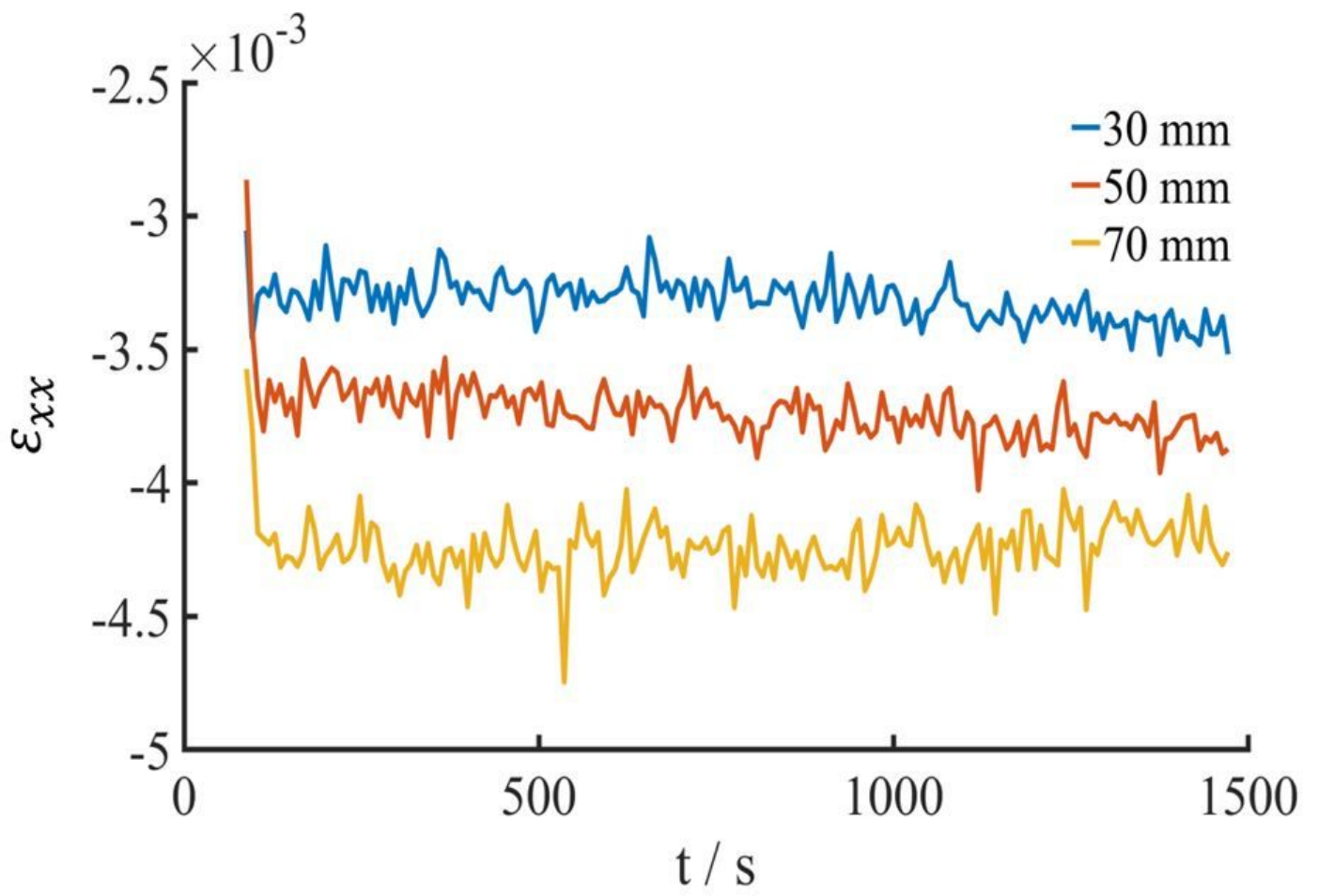


Figure 10

Variations of the strain component ϵ_{xx} over time at different sites

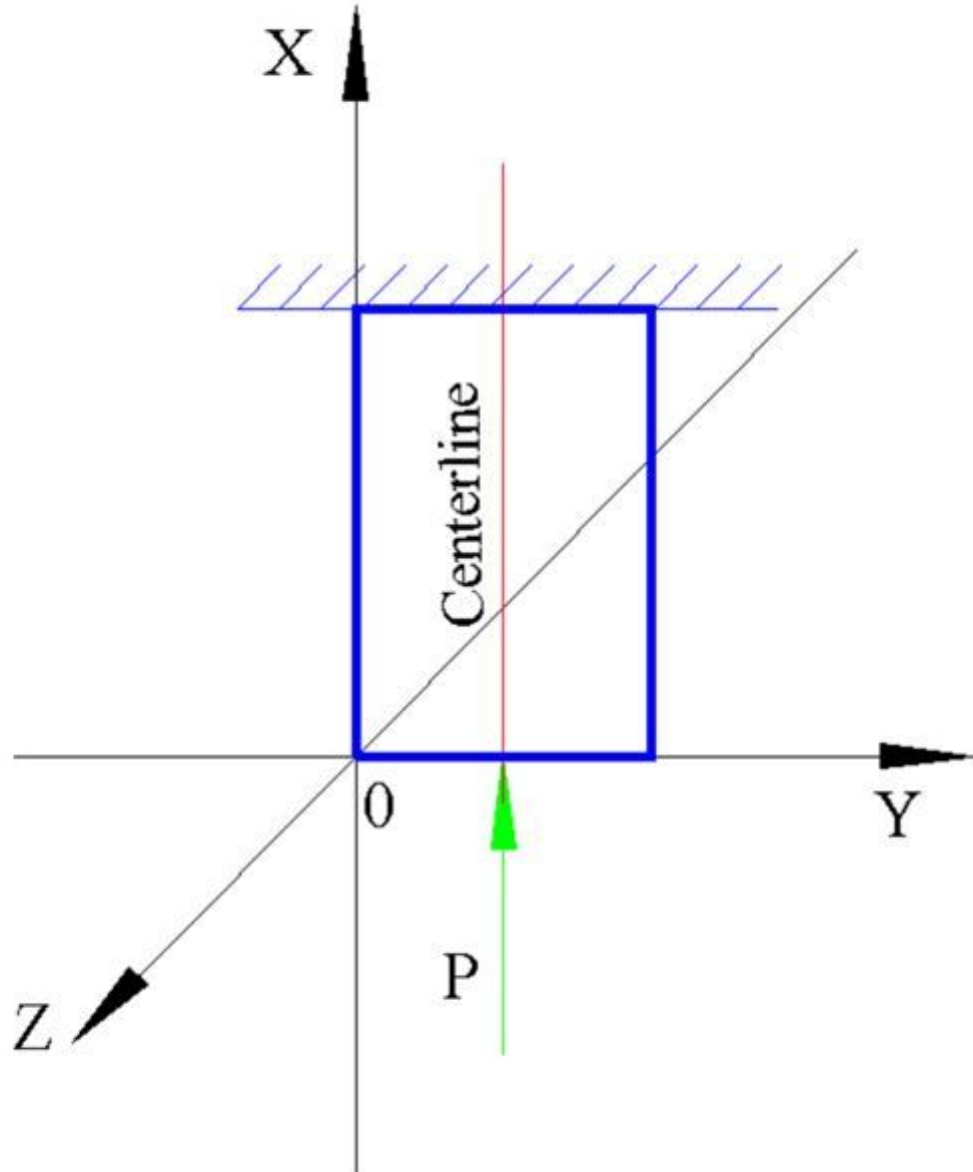


Figure 11

The loading scheme of rock samples

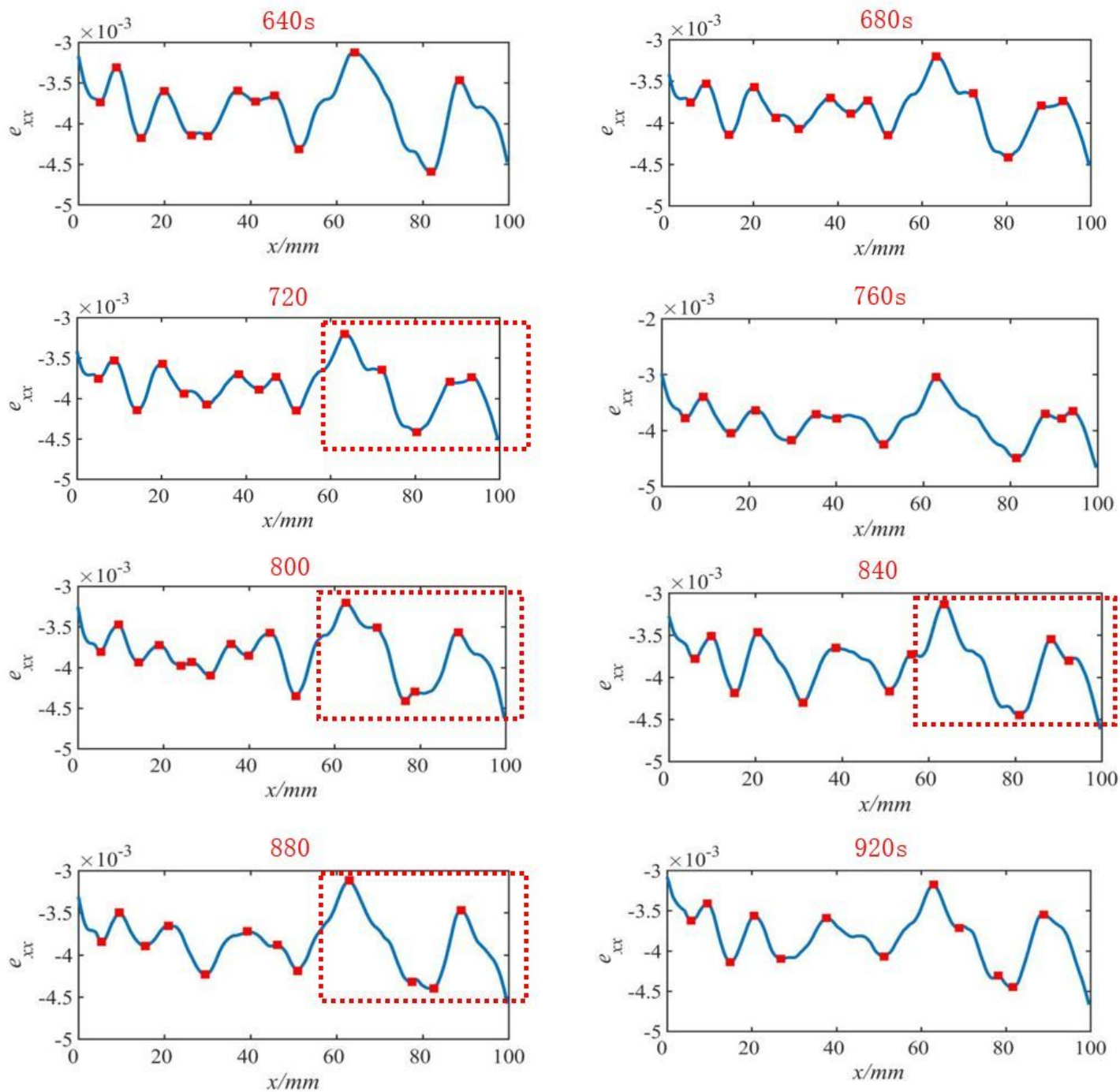


Figure 12

Deformation waves along the central line of the samples from 640s to 920s

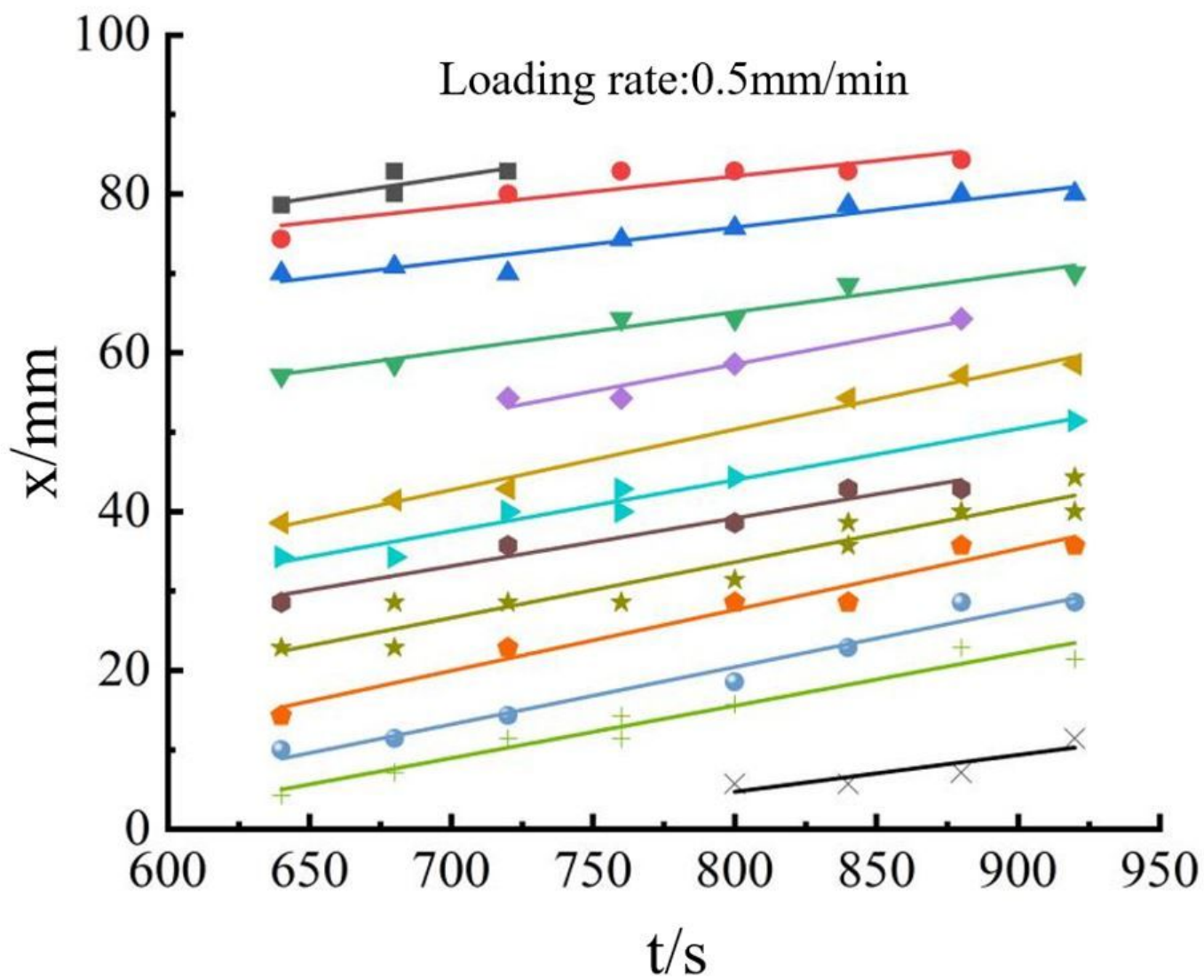


Figure 13

Variation trend of the maximum value of localized strain along the central line

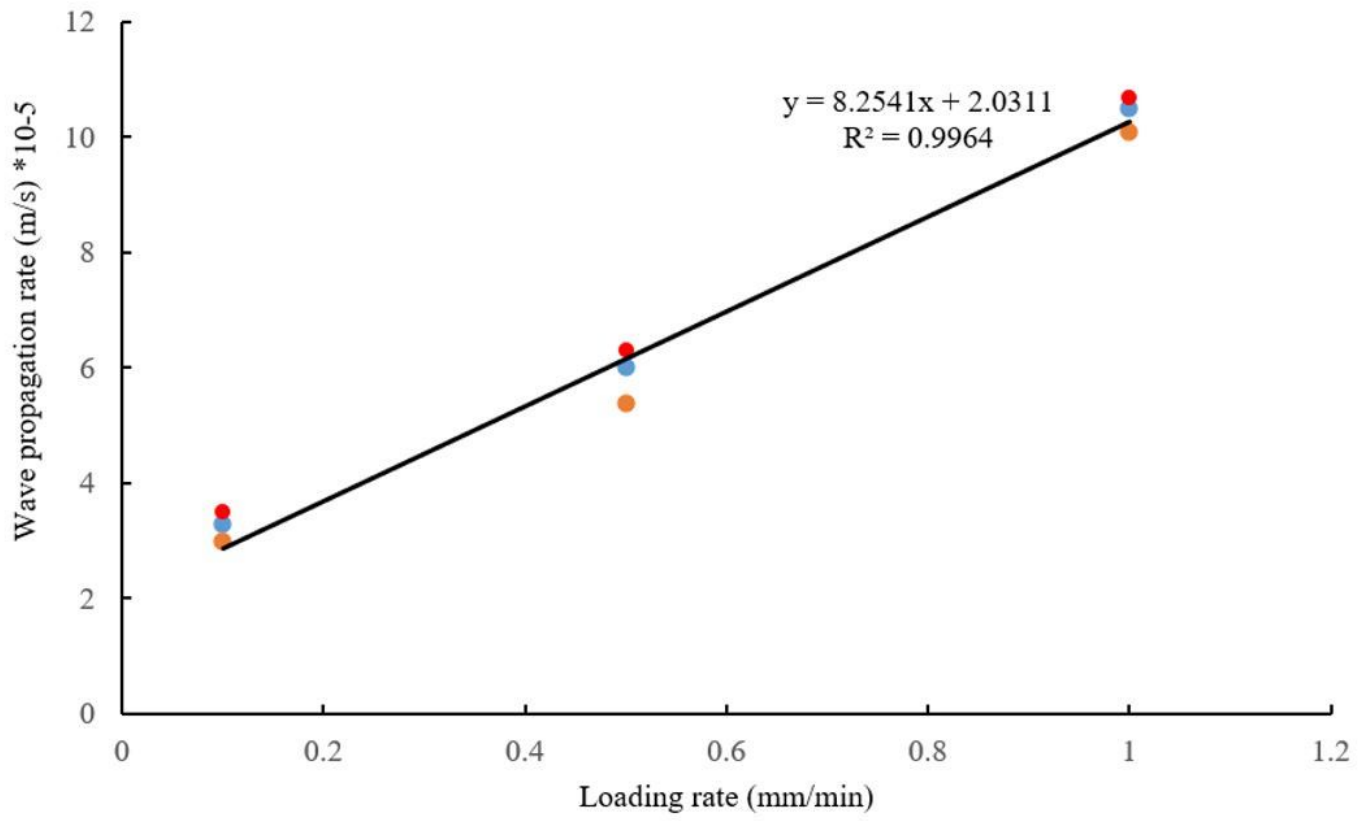


Figure 14

Dependence of the propagation rate of the deformation waves on loading rate